Altered DNA repair pathway engagement by engineered CRISPR-Cas9 nucleases

Vikash P. Chauhan [1,2], Phillip A. Sharp [1,2*], and Robert Langer [1,3*]

[1] *Koch Institute for Integrative Cancer Research, Massachusetts Institute of Technology, Cambridge, MA 02139, USA.*

[2] *Department of Biology, Massachusetts Institute of Technology, Cambridge, MA 02139, USA.*

[3] *Department of Chemical Engineering, Massachusetts Institute of Technology, Cambridge, MA 02139, USA.*

** Correspondence to: sharppa@mit.edu (PAS), rlanger@mit.edu (RL)*

CRISPR-Cas9 introduces targeted DNA breaks that engage competing DNA repair pathways, producing a spectrum of imprecise insertion/deletion mutations (indels) and precise templated mutations [1,2]. The relative frequencies of these pathways are thought to primarily depend on genomic sequence and cell state contexts, limiting control over mutational outcomes [3,4]. Here we report engineered Cas9 nucleases that engage competing repair pathways at dramatically altered frequencies. We accordingly designed a Cas9 variant (vCas9) that suppresses otherwise dominant small indels produced by nonhomologous end-joining (NHEJ) repair. Instead, vCas9 makes repair pathways utilizing homologous sequences dominant, specifically indel-producing microhomology-mediated end-joining (MMEJ) and precise templated mutation-producing homology-directed repair (HDR). Consequently, vCas9 enables efficient precise templated mutations in dividing and non-dividing cells – establishing a new paradigm of targeted nucleases custom-designed for specific mutational applications.

Genome editing with CRISPR-Cas9 harnesses cellular double-strand break (DSB) repair pathways, such as non-homologous end-joining (NHEJ), microhomology-mediated end-joining (MMEJ), and homology-directed repair (HDR), to mutate targeted loci [1,2]. NHEJ produces semi-random insertion/deletion mutations (indels) that are generally small. In contrast, MMEJ makes sequence-specific indels that can be small or large by using small homologous sequences flanking the DSB. Meanwhile, HDR utilizes a homologous DNA repair template that recombines with the DSB site to create specific mutations called precise edits. These repair pathways compete to repair each DSB due to multi-faceted regulation [5–9], though NHEJ is the dominant mechanism [10,11]. The relative frequencies of these repair pathways and the mutations they produce follow a predictable distribution that is thought to be defined by the sequence of the targeted locus and the cell state [3,4]. A central goal of the field is to develop means for controlling the relative frequencies of particular repair pathways, primarily with the aim of making precise editing by HDR or specific indels by MMEJ more frequent. This requires understanding what underlies competition between repair pathways and accordingly designing strategies to redirect DNA repair.

To provide a better understanding of how DNA repair pathways compete at Cas9-induced DSBs, we first studied how indels are outcompeted by templated precise edits. We contrasted indel distributions of wild-type *S. pyogenes* Cas9 without or with an HDR template at several loci in HEK293T cells. Using deep next-generation sequencing of the amplified loci, we determined the frequencies of different sizes and types of indels and templated precise edits (Extended Data Fig. 1a). Remarkably, the degree to which precise editing outcompetes an indel was strongly correlated with indel size (Extended Data Fig. 1b). Moreover, there were differences between how indels produced through different pathways competed with precise edits. MMEJ deletions were more effectively outcompeted by precise edits than NHEJ deletions while NHEJ insertions were not significantly affected (Extended Data Fig. 1c). Since the majority of indels produced by Cas9 were small NHEJ-based indels, this was the major source of competition for precise editing by HDR.

We hypothesized that a Cas9 variant that produces larger indels by promoting MMEJ over NHEJ would also enable greater HDR template utilization. While no Cas9 variants are known to alter the relative frequencies of different repair pathways, natural and engineered Cas9 variants produce varied DSB structures following cutting [12,13] and DSB structure influences repair mechanisms [14,15]. These engineered variants have mutations in residues located at the DNA substrate interface of Cas9. Accordingly, we explored whether mutating Cas9 residues at the DNA substrate interface could alter the relative frequencies of different repair pathways engaged by Cas9 (Fig. 1a,b). To test this, we selected residues with known or proposed interactions with the substrate strands [16–18]. These fourteen residues were either basic or polar and we mutated each to a hydrophobic Alanine to reduce putative DNA interactions (Fig. 1c and Extended Data Fig. 2). To measure precise editing and indel frequency for these mutants, we combined them with HDR templates that produce small sequence replacements at the *EMX1* and *CXCR4* loci in HEK293T cells (Fig. 1b) and analyzed alterations using Sanger sequencing of the amplified locus with TIDE analysis [19]. Several of the Cas9 single-mutants reduced the frequency of indels while increasing precise editing frequency (Fig. 1d and Extended Data Fig. 3a). We then combined the mutant residues that most changed repair outcomes from the single-mutants into double- and triple-mutants and

identified several mutant combinations that significantly increased precise editing frequency and reduced indel frequency relative to wild-type Cas9 (Fig. 1d and Extended Data Fig. 3a). We tested these engineered Cas9 variants by applying HDR to convert a green fluorescent protein (GFP) transgene inserted in the genome of HEK293T cells to blue fluorescent protein (BFP) [20]. One variant, R976A-K1003A, most effectively increased precise editing frequency while decreasing indel frequency (Extended Data Fig. 3b-d). Yet while this variant greatly altered the frequency of these competing repair pathways, its total editing activity was lower than that of wild-type Cas9 at all loci tested.

To address this challenge, we investigated whether the lost total editing activity could be rescued by additional mutations. The R976A mutation produced the greatest change in repair pathway frequency along with the largest drop in total editing activity and sits at one end of the nontarget cleft near where the substrate DNA strands separate (Fig. 1e). We thought that R976 might regulate repair pathway frequency by affecting how the nontarget strand sits in its cleft and where it is cut, while also controlling total activity by aiding in substrate strand separation prior to cutting. To test whether mutating residues nearby A976 to Arginine could rescue activity without reverting changes to repair pathway frequency, we mutated six residues in the R976A-K1003A variant to produce a set of triple-, quadruple-, and quintuple-mutants (Fig. 1e). We assessed these new variants using a similar HDR assay at the *VEGFA* and *EMX1* loci in HEK293T cells and analyzed using Sanger sequencing and TIDE analysis (Fig. 1b). This led to one variant, S55R-R976A-K1003A-T1314R, that maximally rescued activity approaching that of wild-type Cas9 (Fig. 1f and Extended Data Fig. 3e). Importantly, this variant did not increase non-specific genome activity but surprisingly improved on-target versus off-target editing specificity compared to wild-type Cas9 (Extended Data Fig. 4). Since Cas9$^{S55R\text{-}R976A\text{-}K1003A\text{-}T1314R}$ was the most intriguing and active variant of Cas9, we named it vCas9.

To clarify the mechanisms by which the above variants alter DNA repair pathway frequency, we studied editing outcomes for each engineered Cas9 variant from our Alanine substitution screen. There was a strong correlation between precise editing frequency and mean indel size for Cas9 variants (Extended Data Fig. 5a,b). We then analyzed indel distributions and mechanisms for wild-type Cas9 and vCas9 at

several loci in HEK293T cells using deep next-generation sequencing (Fig. 2a and Extended Data Fig. 5c-e). We found that vCas9 induced indels of larger size than those by wild-type Cas9 (Fig. 2b) and greatly suppressed NHEJ deletions and insertions while promoting MMEJ deletions (Fig. 2c). Specifically, vCas9 shifted indels from NHEJ repair to MMEJ repair utilizing larger microhomologies, suggesting enhanced DNA end resection or strand separation (Fig. 2c). In the presence of an HDR template, vCas9 consistently made HDR dominant, with the remaining minor repair outcomes comprised mostly of NHEJ insertions and MMEJ deletions (Fig. 2d). We also assessed wild-type Cas9 and vCas9 repair frequencies following treatment of HEK293T cells with inhibitors of MMEJ (Rucaparib) or NHEJ (NU7026). Inhibiting NHEJ combined with wild-type Cas9 led to editing patterns that resembled vCas9, while inhibiting MMEJ largely ablated editing by vCas9 but not wild-type Cas9 (Fig. 2e and Extended Data Fig. 5f). Comparing repair frequencies without or with an HDR template showed that vCas9 also increased the degree to which precise editing outcompeted any size indel (Fig. 2f). Together, these data demonstrate that vCas9 suppressed NHEJ in favor of repair pathways that use homologous sequences, hence promoting HDR or MMEJ.

We next explored the robustness of these effects on DNA repair pathway frequency with respect to diverse editing contexts. To clarify sequence dependence, we assessed editing at several loci in HEK293T cells using HDR templates producing small edits with analysis by deep next-generation sequencing. Reassuringly, vCas9 significantly and consistently altered DNA repair pathway frequency at all loci (Fig. 3a). We also assessed whether vCas9-produced edits are precise and functional by again applying HDR to convert a GFP transgene to BFP. Indeed, vCas9 greatly increased precise gene conversion while suppressing indel frequency (Fig. 3b,c). To examine cell-type dependence, we applied similar HDR templates to produce small edits at several loci in HeLa, A549, and Panc1 cells. In each cell model and locus, vCas9 consistently altered precise editing and indel frequencies (Fig. 3d and Extended Data Fig. 6). We further tested two other precise edit types of interest, large insertions from double-stranded templates and untemplated precise collapse of duplications [4]. For both edit types, vCas9

similarly favored precise editing and suppressed indels (Fig. 3e,f). These data indicate that vCas9 robustly suppressed indels and promoted precise editing across varied loci, cells, and edit types.

A major limitation of CRISPR technology for precise editing to generate genetic models or treat certain diseases is the lack of HDR in non-dividing cells [11,21]. In contrast, MMEJ and NHEJ are active in non-dividing cells [11,22]. To address this, we next investigated whether vCas9 might produce precise editing in non-dividing cells by developing an MMEJ-driven templated strategy. This method, termed microhomology-directed recombination (MDR), utilizes partially double-stranded DNA templates with single-stranded microhomology arms complementary to sequences distal to the DSB ends (Fig. 4a). These MDR templates putatively enable replacements of small segments of genomic DNA situated between the two microhomology arms. We tested MDR in HEK293T cells using the GFP to BFP gene conversion assay with varied MDR template designs (Extended Data Fig. 7a). We found that the MDR templates enabled efficient precise editing, with large increases in precise editing frequency when using vCas9 as compared to wild-type Cas9 (Extended Data Fig. 7b,c). Under the same conditions, MDR generated a variety of precise edit types including substitutions, insertions, and deletions, as analyzed by deep next-generation sequencing (Fig. 4a). For each type of precise edit, vCas9 greatly increased precise editing frequency (Fig. 4b). Considering these findings, we tested MDR in quiescent primary human dermal fibroblasts, an established model of G0 non-dividing cells [23]. Following induction of quiescence in these fibroblasts over seven days (Extended Data Fig. 8), we assessed MDR for making small precise edits (Fig. 4a). We found that these precise edits were more frequent than all other types of edits in these cells (Fig. 4c). Furthermore, precise editing with vCas9 compared favorably to outcomes achieved by prime editing (Extended Data Fig. 9) [24]. This was probably because vCas9-generated DSBs near-completely precluded other pathways leading to domination by precise editing.

To our knowledge, this is the first demonstration that CRISPR-Cas9 can be engineered to alter its propensity for different pathways of DSB repair. We have shown that vCas9 suppresses NHEJ and promotes pathways that enable precise editing, such as HDR and MMEJ. These changes are not subtle, with a pronounced shift in the dominant repair pathway from NHEJ to HDR or MMEJ. Furthermore, we

have shown that vCas9 makes efficient precise edits in non-dividing cells by MMEJ. These properties could possibly make vCas9 an important tool for molecular genetics and gene therapy. This work also serves as a potential guide for future engineering efforts to improve the function of Cas9 and related programmable nucleases. Indeed, our findings demonstrate the importance of studying how natural and engineered nucleases engage different repair pathways. Future efforts may lead to diverse libraries of nucleases, each specialized to producing a particular set of mutational outcomes. Along these lines, this work may establish a new paradigm for genome editing in which a particular desired edit might be matched with a custom-engineered nuclease that predominantly produces that edit.

Figures

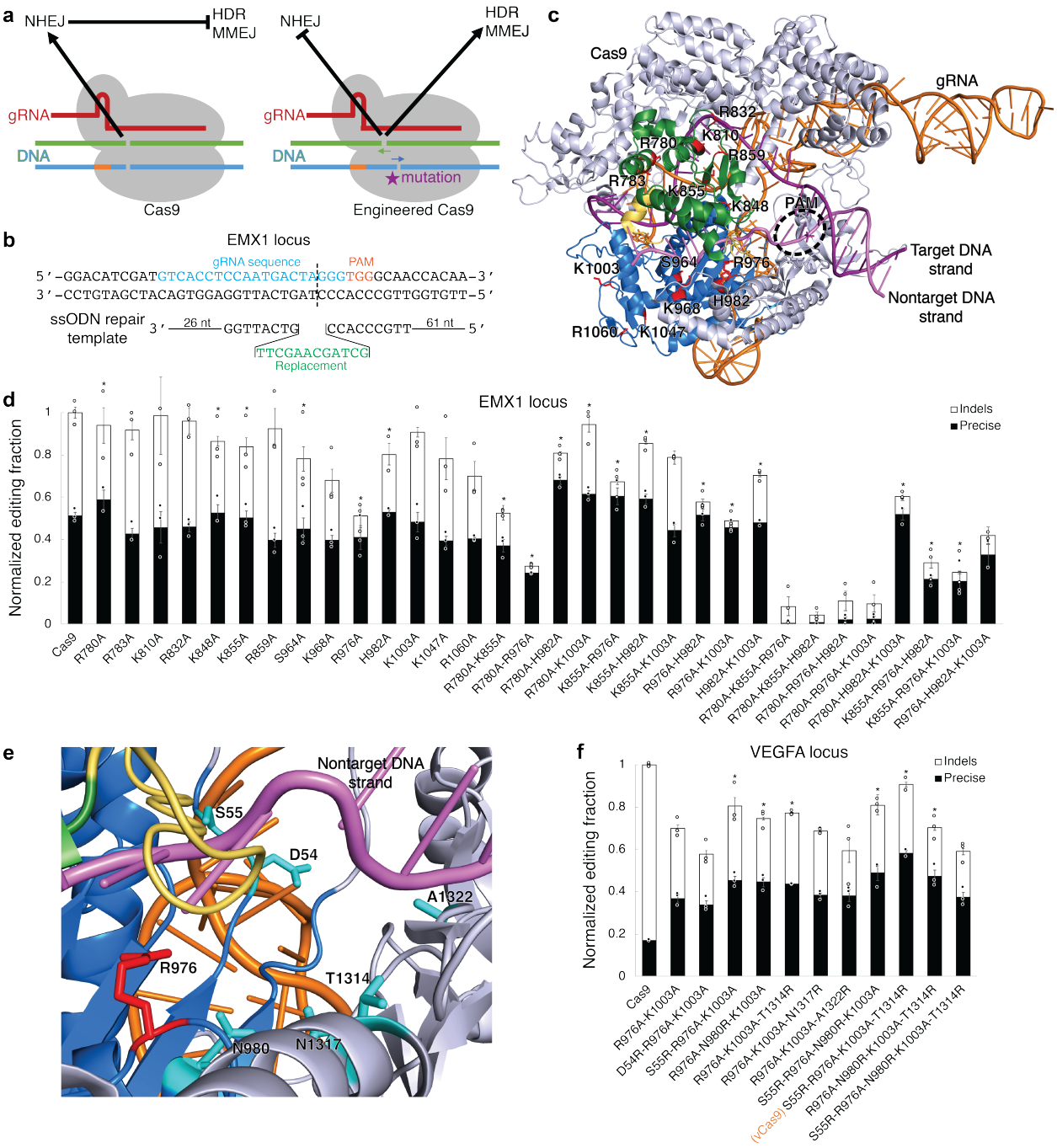

Figure 1. Design of Cas9 variants with altered repair pathway frequencies. a, Model of the balance between NHEJ and HDR or MMEJ repair pathways for Cas9 variants. **b**, Design of a gRNA and HDR template to introduce a precise edit. **c**, Cas9 residues at the interface with the substrate DNA strands that were selected for Alanine substitution and altered repair pathway screening. The mutated residues (red) are located in either the mobile HNH domain (green) or the immobile RuvC domain (blue), which are

connected by linker segments (yellow). **d**, Screen of precise editing and indel frequencies for engineered Cas9 variants using an HDR template. **e**, Cas9 residues proximal to R976 were selected for Arginine substitution and activity rescue screening. The mutated residues (teal) are located near the nontarget substrate DNA strand (pink). **f**, Screen of precise editing and indel frequencies for engineered Cas9 variants using an HDR template. * indicates $p < 0.05$ for precise editing frequency compared to wild-type Cas9 in **d**, or for total editing frequency compared to wild-type Cas9 in **f**. Data were analyzed by Sanger sequencing and represent means of n = 2-3 independent replicates with standard errors.

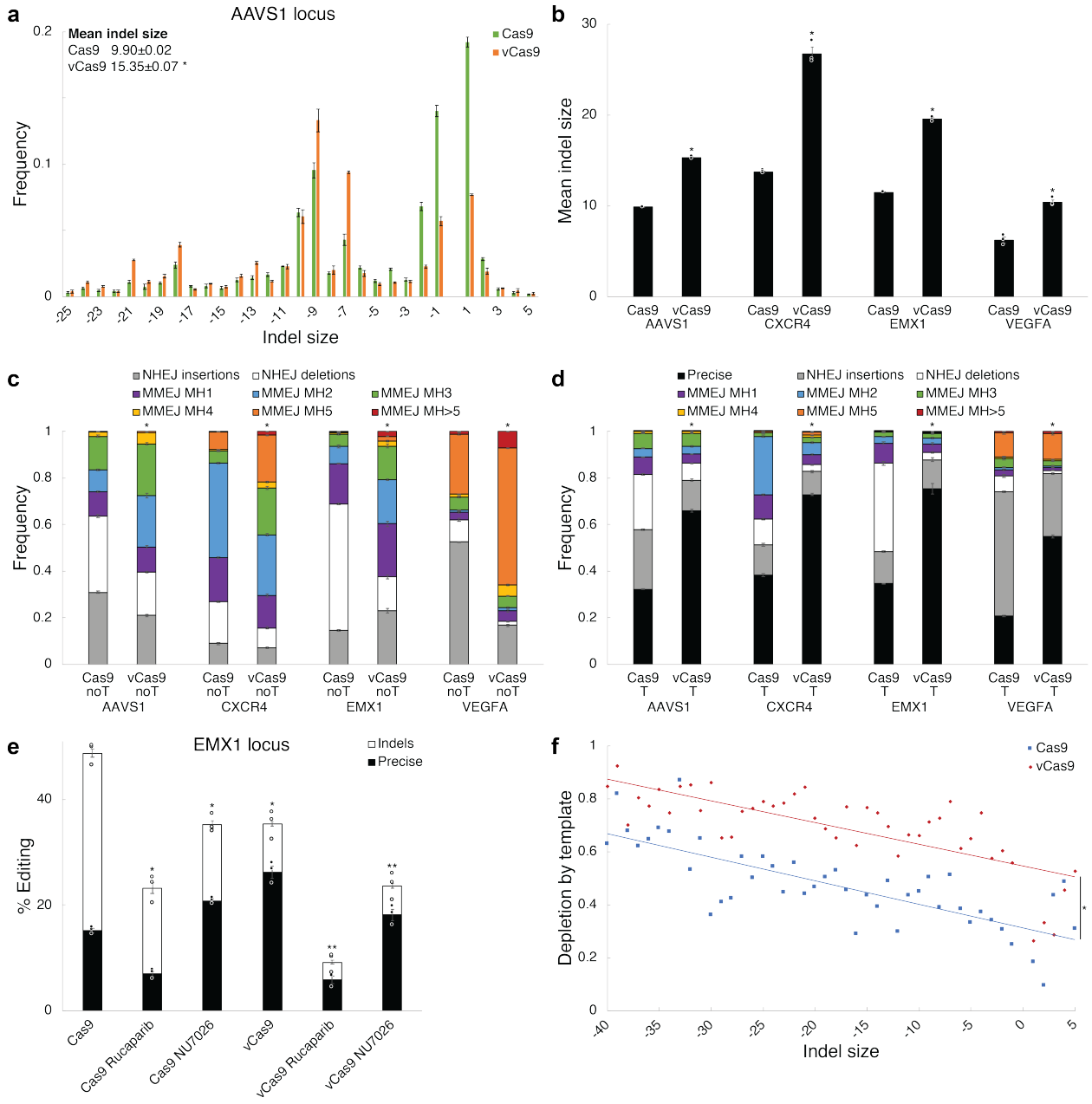

Figure 2. vCas9 suppresses NHEJ and makes MMEJ or HDR dominate repair outcomes. a, Distributions of indel sizes induced. **b**, Mean indel size induced at several loci. **c**, **d**, Frequencies of repair pathways engaged (**c**) without (noT) and (**d**) with (T) a repair template at several loci. NHEJ mutations are subset into insertions or deletions, while MMEJ mutations are subset by microhomology length (MH1 to MH>5). **e**, Precise editing and indel frequencies using HDR templates without or with an MMEJ inhibitor (Rucaparib) or NHEJ inhibitor (NU7026). **f**, Degree of depletion by a repair template for indels of different sizes averaged over several loci. The fraction depleted is increased by vCas9 at all indel sizes. * indicates $p < 0.05$ for precise editing frequency compared to wild-type Cas9, ** indicates $p < 0.05$ for precise

editing frequency compared to vCas9. Data were analyzed by deep next-generation sequencing and represent means of $n = 3$ independent replicates with standard errors.

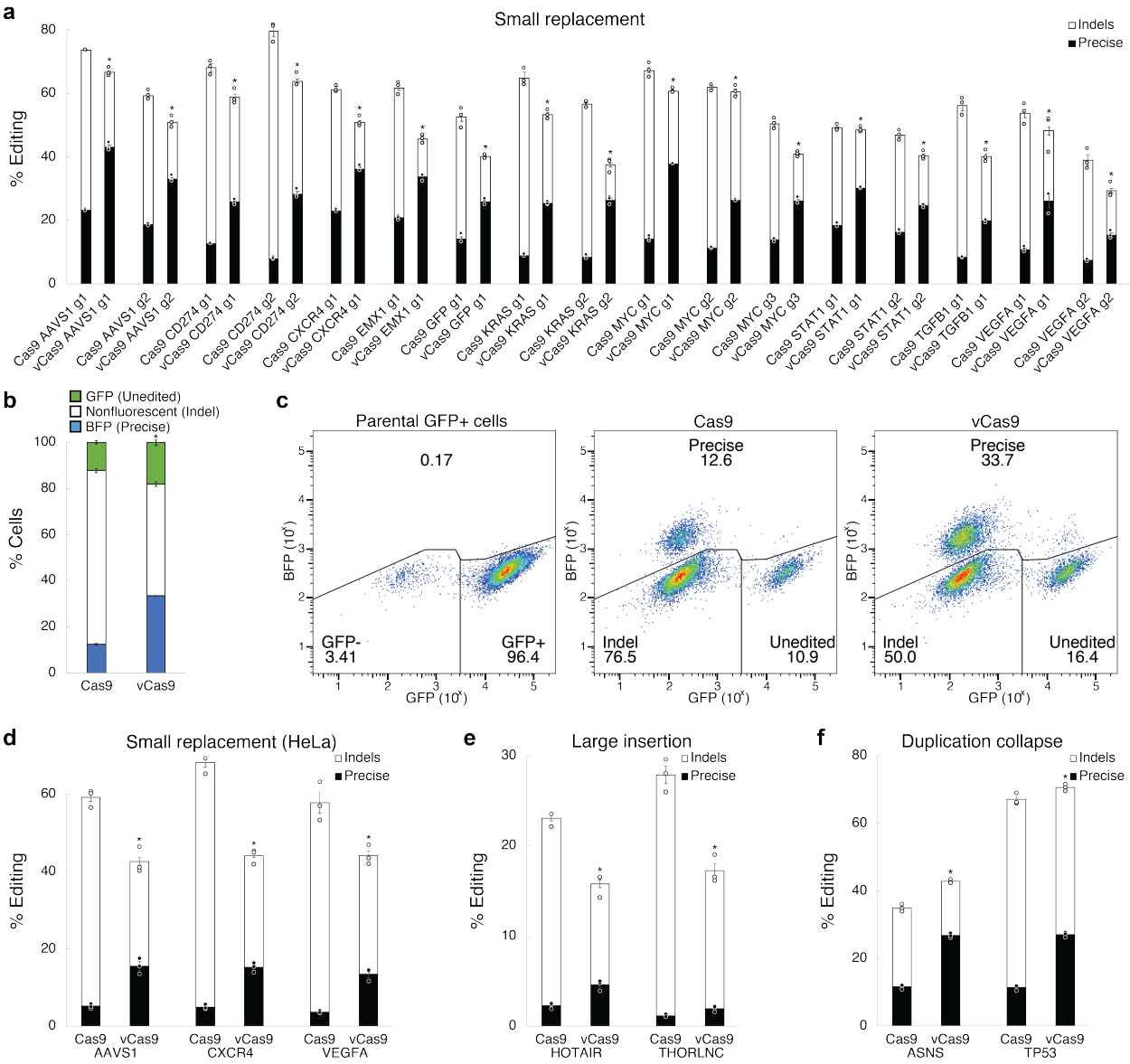

Figure 3. vCas9 enhances precise editing and suppresses indels across diverse editing contexts. **a**, Precise editing and indel frequencies using small replacement (1-10 bp) HDR templates at several loci. **b**, Frequency of precise gene conversion from GFP to BFP. **c**, Flow cytometry plots showing BFP-positive (indicating precise edits), nonfluorescent (indicating indels), and GFP-positive (indicating unedited cells) cell population fractions. **d**, Precise editing and indel frequencies using small replacement (1-10 bp) HDR templates at several loci in HeLa cells. **e**, Precise editing and indel frequencies using large insertion (~50 bp) templates at several loci. **f**, Precise editing and indel frequencies for untemplated collapse of duplications (10-20 bp) at several loci. * indicates $p < 0.05$ for precise editing frequency compared to wild-type Cas9. Data were analyzed by deep next-generation sequencing in **a**, **d-f** or flow cytometry in **b**, **c** and represent means of $n = 3$ independent replicates with standard errors.

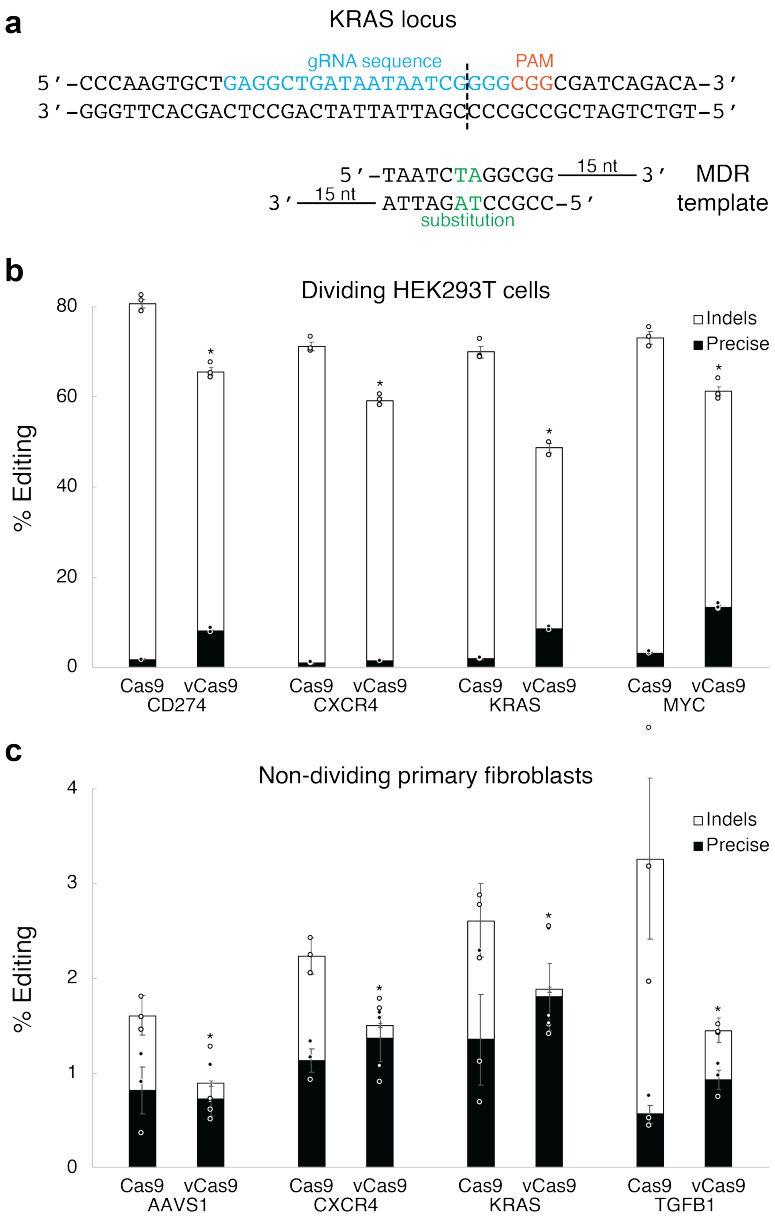

Figure 4. vCas9 enables efficient precise editing through MMEJ in dividing and non-dividing cells. **a**, Design of a gRNA and MDR template to introduce a precise edit. **b**, Precise editing and indel frequencies using MDR templates in dividing HEK293T cells. **c**, Precise editing and indel frequencies using MDR templates in non-dividing (quiescent) primary human dermal fibroblasts. * indicates $p < 0.05$ for precise editing frequency compared to wild-type Cas9. Data were analyzed by deep next-generation sequencing and represent means of $n = 3$ independent replicates with standard errors.

Extended Data

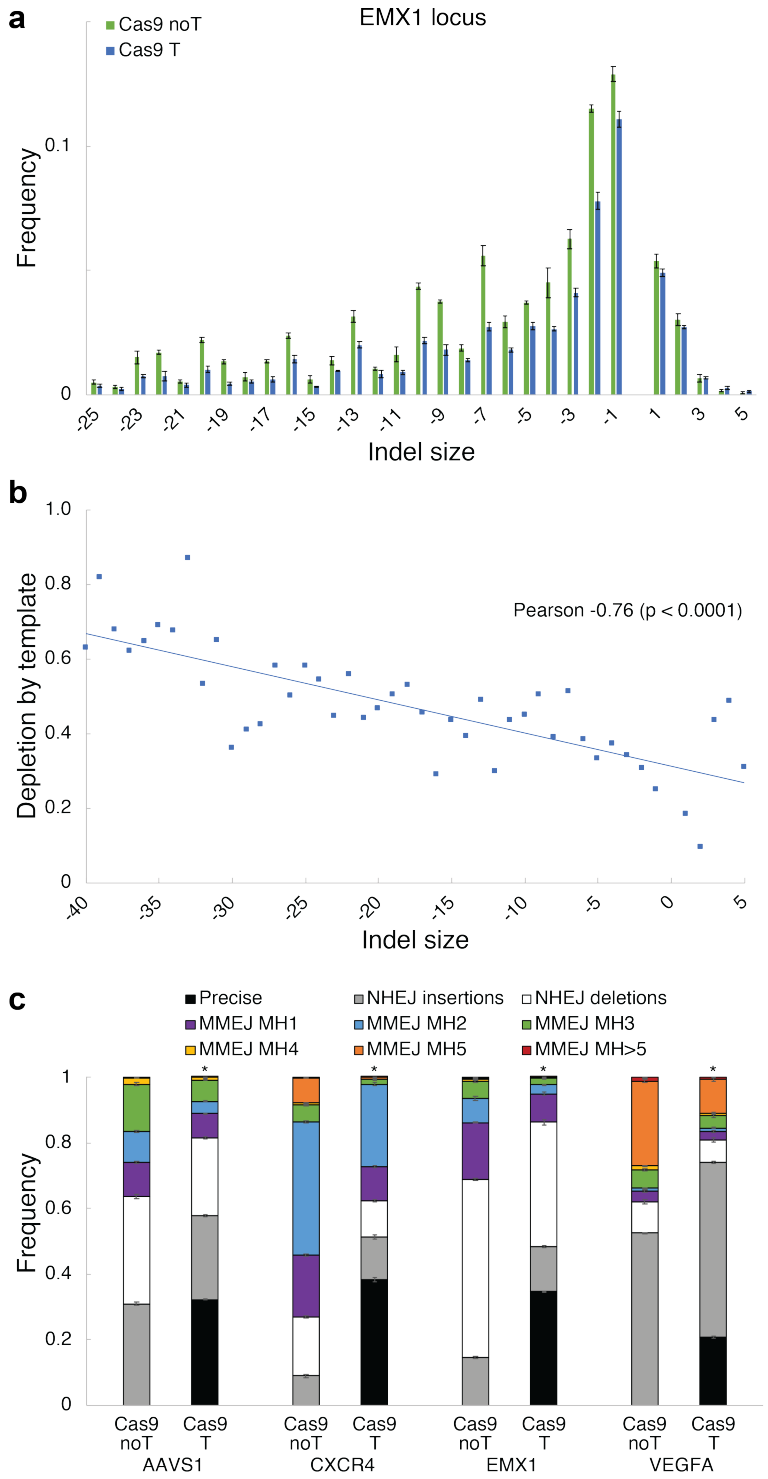

Extended Data Figure 1. Templated precise editing with Cas9 is outcompeted by small indels produced by NHEJ. a, Distributions of indel sizes induced without (noT) or with (T) a repair template. **b**, Degree of depletion by a repair template for indels of different sizes averaged over several loci. The

longer the indel size the greater the depletion. **c**, Frequencies of repair pathways engaged without (noT) or with (T) a repair template at several loci. NHEJ mutations are subset into insertions or deletions, while MMEJ mutations are subset by microhomology length (MH1 to MH>5). * indicates $p < 0.05$ for frequency compared between noT and T in **c**. Data were analyzed by deep next-generation sequencing and represent means of $n = 3$ independent replicates with standard errors.

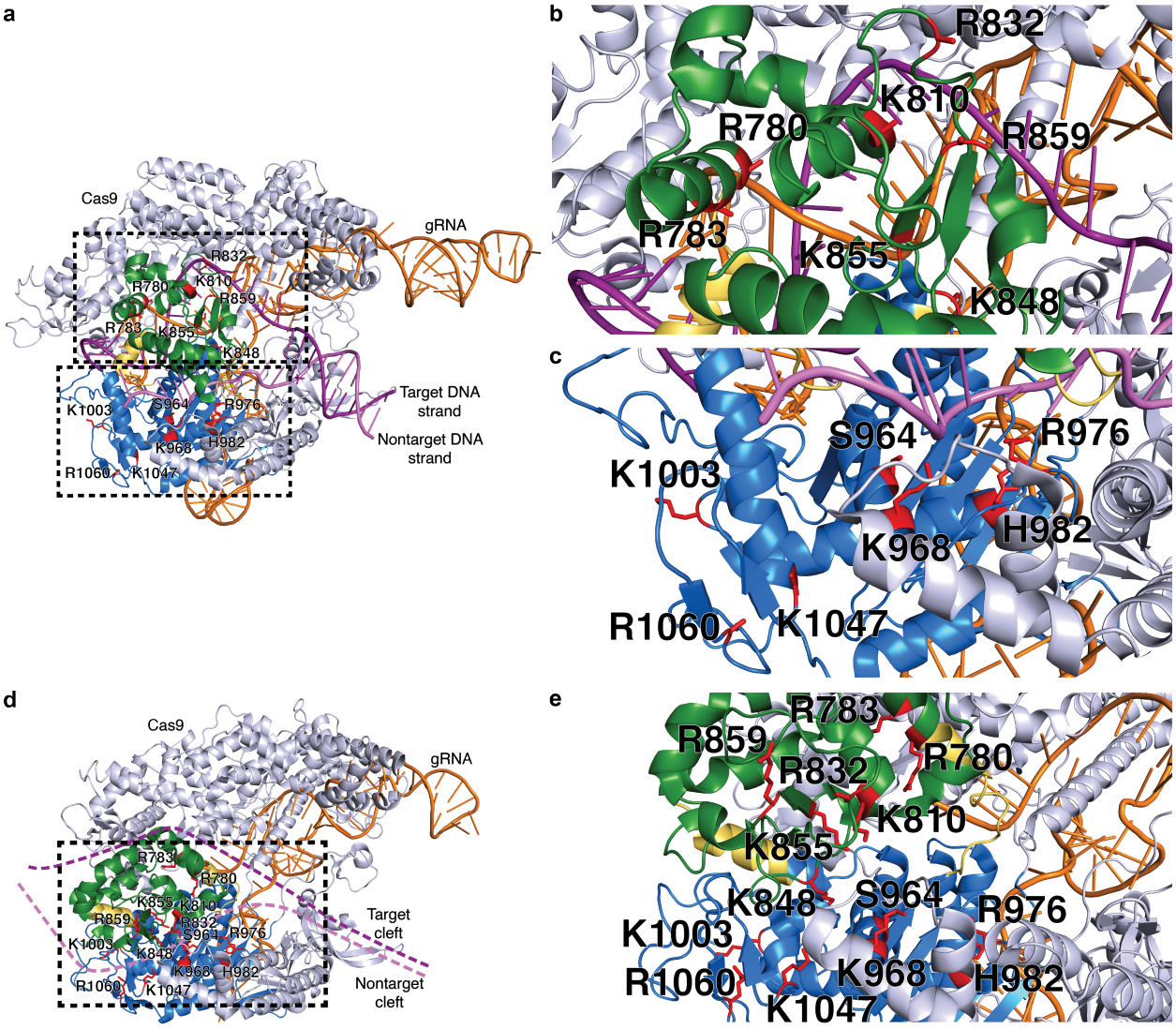

Extended Data Figure 2. Detailed views of mutated Cas9 residues. a, Wide view of Cas9 residues at the interface with the substrate DNA strands that were selected for mutation and screening. The mutated residues (red) are located in either the mobile HNH domain (green) or the immobile RuvC domain (blue), which are connected by linkers (yellow). **b**, Focused view of the residues from **a** in the target cleft. **c**, Focused view of the residues from **a** in the nontarget cleft. **d**, Location of the same Cas9 residues in a structure of Cas9 without the DNA substrate bound. **e**, Focused view of the residues from **d** in the nontarget cleft.

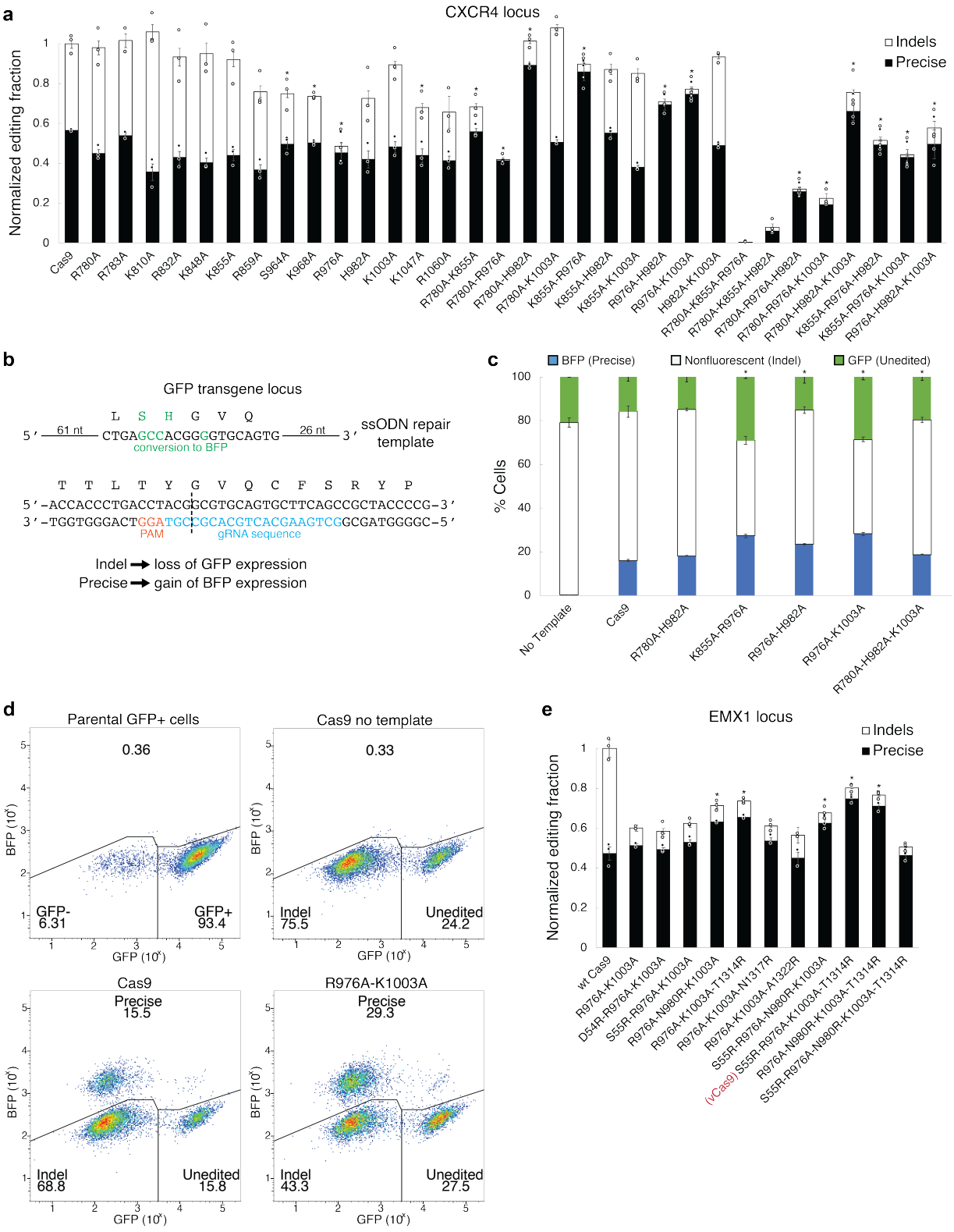

Extended Data Figure 3. Rational engineering produces Cas9 variants with increased HDR frequency. a, Screen of precise editing and indel frequencies for engineered Cas9 variants using an

HDR template. **b**, Design of a gRNA and HDR template to introduce a GFP to BFP conversion. **c**, Frequency of precise gene conversion from GFP to BFP. **d**, Flow cytometry plots showing BFP-positive (indicating precise edits), nonfluorescent (indicating indels), and GFP-positive (indicating unedited cells) cell population fractions. **e**, Screen of precise editing and indel frequencies for engineered Cas9 variants using an HDR template. * indicates $p < 0.05$ for precise editing frequency compared to wild-type Cas9 in **a**, **c** or for total editing frequency compared to wild-type Cas9 in **e**. Data were analyzed by Sanger sequencing in **a**, **e** or flow cytometry in **c**, **d** and represent means of $n = 3$ independent replicates with standard errors.

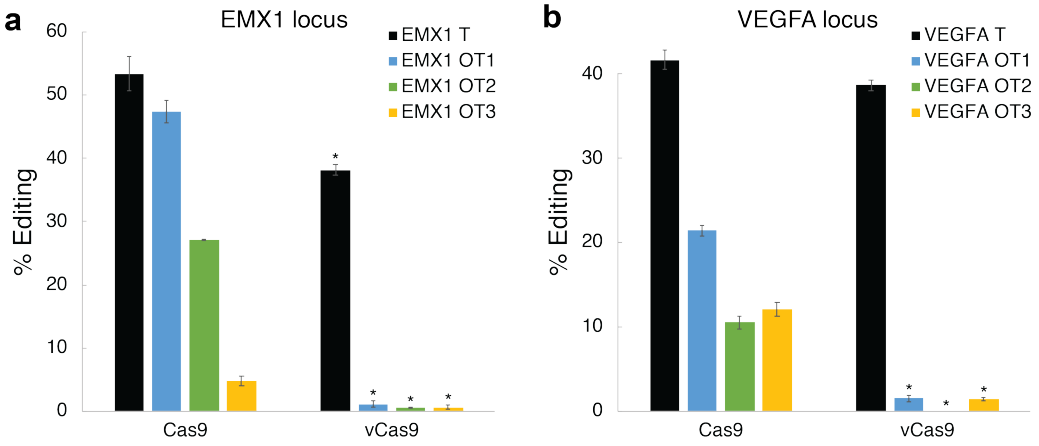

Extended Data Figure 4. vCas9 improves on-target versus off-target editing specificity. a, **b**, Indel frequencies at on-target (T) and off-target (OT1-OT3) loci. * indicates $p < 0.05$ for indel frequency compared to wild-type Cas9. Data were analyzed by Sanger sequencing and represent means of n = 2-3 independent replicates with standard errors.

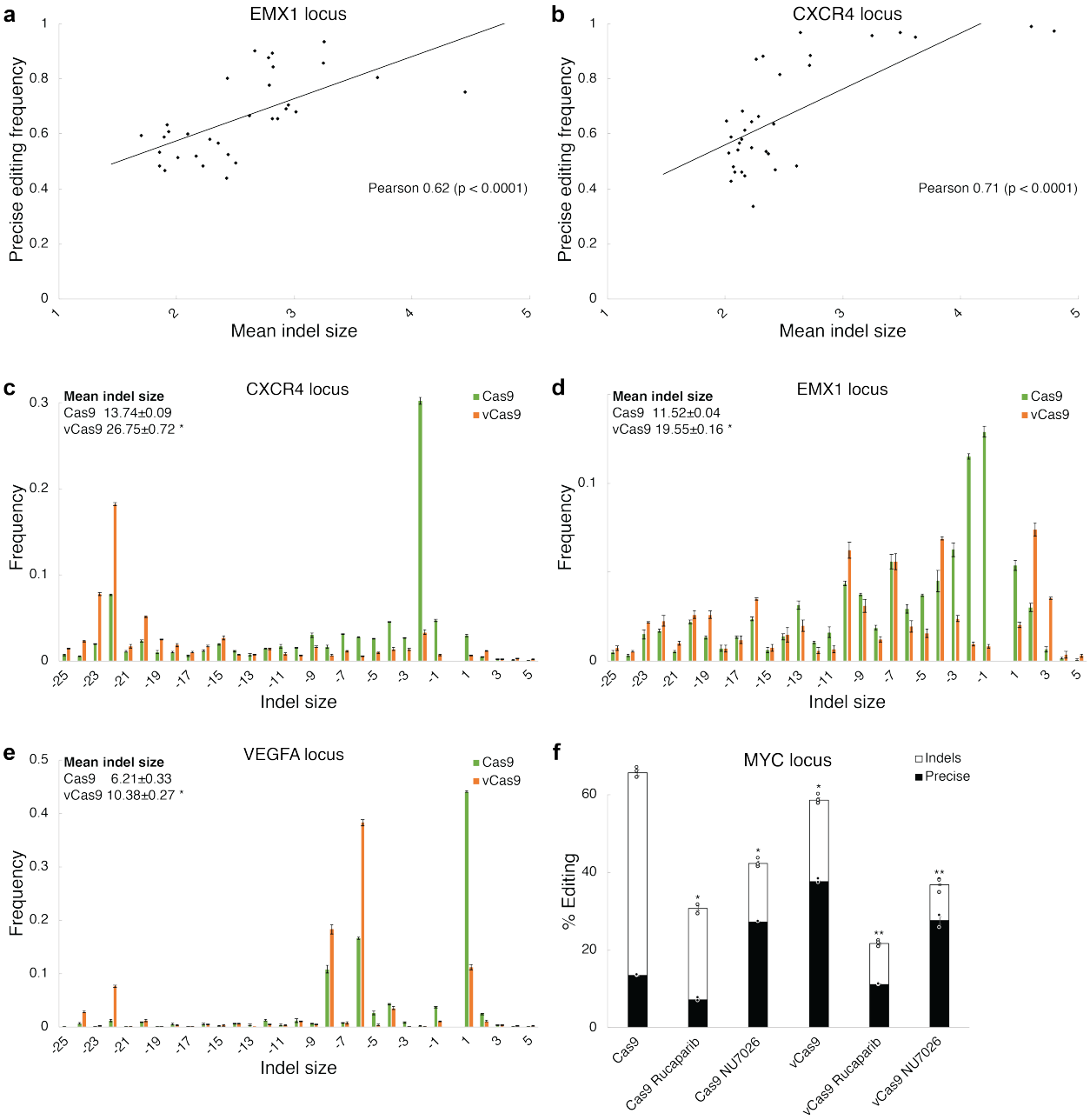

Extended Data Figure 5. Engineered Cas9 variants suppress small NHEJ indels and promote larger MMEJ indels. a, **b**, Correlation between mean indel size (for remaining indels after precise editing) and precise editing frequency using HDR templates across Cas9 variants from the Alanine-substitution screen. **c-e**, Distributions of indel sizes induced. **f**, Precise editing and indel frequencies using HDR templates without or with an MMEJ inhibitor (Rucaparib) or NHEJ inhibitor (NU7026). * indicates $p < 0.05$ for precise editing frequency compared to wild-type Cas9, ** indicates $p < 0.05$ for precise editing frequency compared to vCas9. Data were analyzed by Sanger sequencing in **a**, **b** or deep next-generation sequencing in **c-f** and represent means of n = 2-3 independent replicates with standard errors.

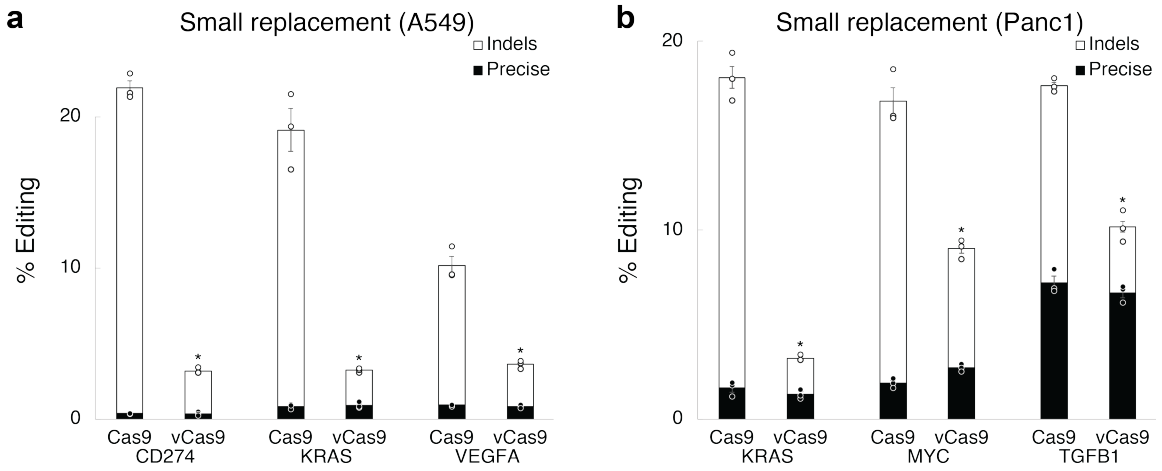

Extended Data Figure 6. vCas9 enhances precise editing and suppresses indels across cell types. **a**, Precise editing and indel frequencies using HDR templates at several loci in A549 cells. **b**, Precise editing and indel frequencies using HDR templates at several loci in Panc1 cells. * indicates $p < 0.05$ for precise editing frequency compared to wild-type Cas9. Data were analyzed by deep next-generation sequencing and represent means of $n = 3$ independent replicates with standard errors.

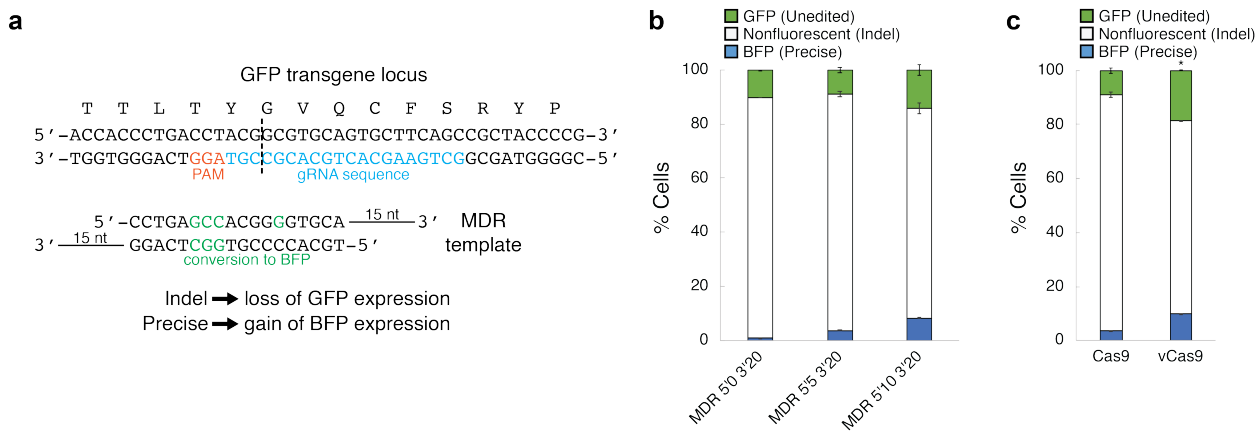

Extended Data Figure 7. MDR enables efficient precise editing through MMEJ. a, Design of a gRNA and MDR template to introduce a GFP to BFP conversion. **b**, Precise editing and indel frequencies using MDR templates with varied microhomology arm lengths (0-10 bp at the 5' ends, 20 bp at the 3' ends). **c**, Frequency of precise gene conversion from GFP to BFP. Data were analyzed by flow cytometry and represent means of $n = 3$ independent replicates with standard errors.

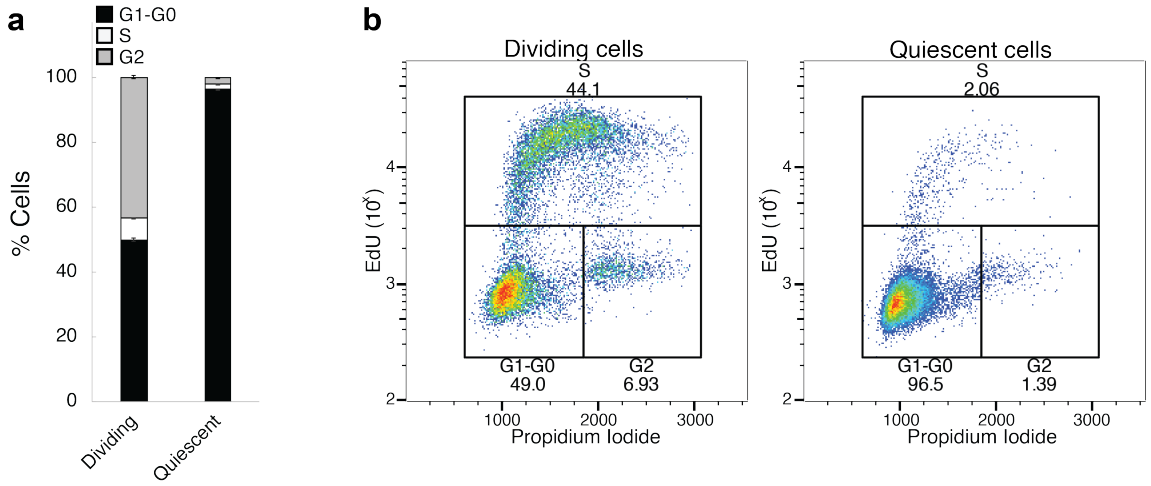

Extended Data Figure 8. Quiescent primary human dermal fibroblasts are nearly all non-dividing. a, Cell cycle profiling of dividing and quiescent primary human dermal fibroblasts. **b**, Flow cytometry plots showing EdU-high (indicating S phase), Propidium Iodide-high (indicating G2 phase), and EdU-low Propidium Iodide-low (indicating G1 or G0 phase) cell population fractions. All data were analyzed by flow cytometry and represent means of $n = 3$ independent replicates with standard errors.

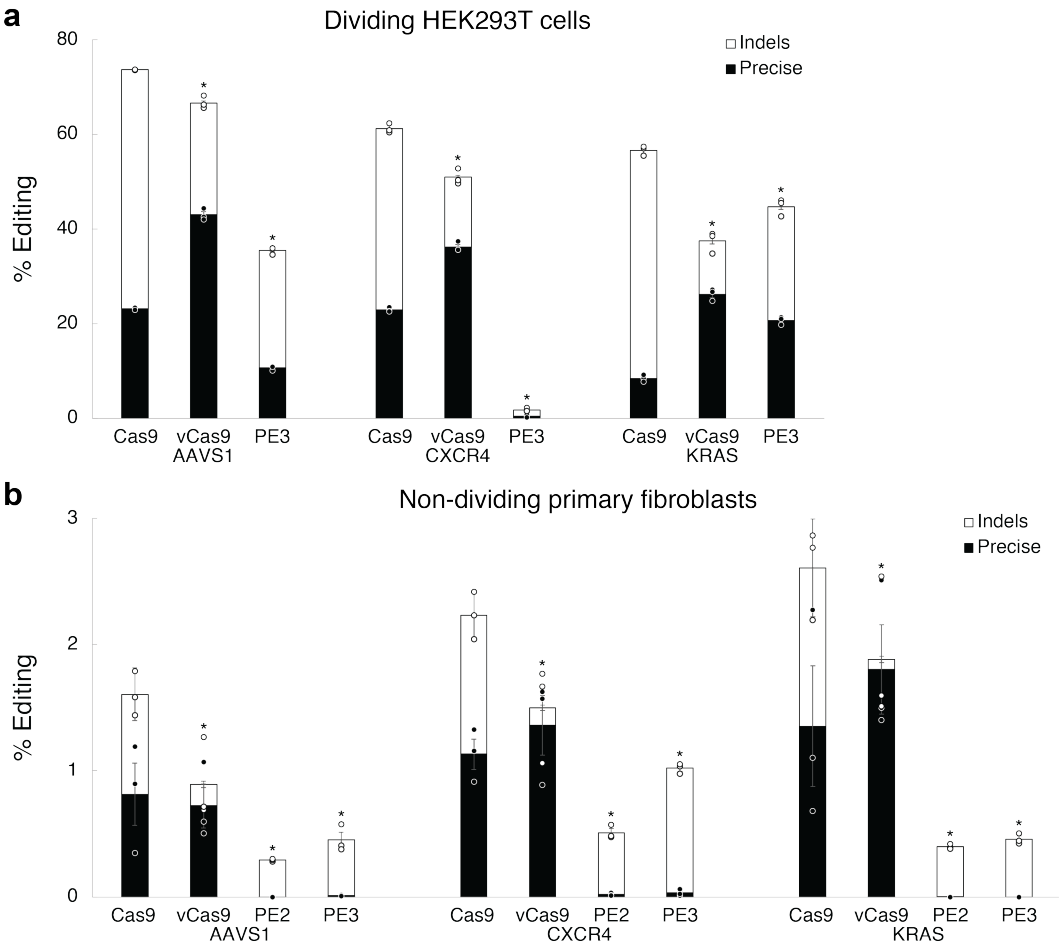

Extended Data Figure 9. vCas9 editing with HDR or MDR compares favorably to prime editing. a, Precise editing and indel frequencies using HDR templates or PE3 prime editing at several loci. **b**, Precise editing and indel frequencies using MDR templates, PE2 prime editing, or PE3 prime editing at several loci in non-dividing (quiescent) primary human dermal fibroblasts. * indicates $p < 0.05$ for precise editing frequency compared to wild-type Cas9. Data were analyzed by deep next-generation sequencing and represent means of $n = 3$ independent replicates with standard errors.

Methods

Mammalian cell culture

All mammalian cell cultures were maintained in a 37ºC incubator at 5% CO_2. HEK293T human embryonic kidney, HeLa human cervical cancer, A549 human lung cancer, Panc1 human pancreatic cancer, and primary human dermal fibroblasts from neonates (GlobalStem) were maintained in Dulbecco's Modified Eagle's Medium with high glucose, sodium pyruvate, and GlutaMAX (DMEM; ThermoFisher, 10569) supplemented with 10% Fetal Bovine Serum (FBS; ThermoFisher, 10438), and 100 U/mL Penicillin-Streptomycin (ThermoFisher, 15140). Primary human dermal fibroblasts were induced to a quiescent state in medium containing 0.1% Fetal Bovine Serum for 7 days [23]. For inhibitor studies, cell media was supplemented with 20 μM Rucaparib (MilliporeSigma, PZ0036) or NU7026 (MilliporeSigma, N1537) dissolved in DMSO (MilliporeSigma, D8418).

Mutagenesis and cloning

Wild-type Cas9 was obtained from pSpCas9 (pX165) and a cloning backbone for gRNA expression was obtained from pX330-U6-Chimeric_BB-CBh-hSpCas9 (pX330), which were gifts from Feng Zhang. Mutagenesis was performed using PCR-driven splicing by overlap extension using primers listed in Supplementary Table 1. Briefly, one fragment was amplified by PCR from pX165 using the cas9-mut-FWD or cas9-mid-FWD and *mutant*-BOT primers and a second fragment was amplified using the *mutant*-TOP and cas9-mid-REV or cas9-mut-REV primers for each mutant. Each pair of fragments was then spliced by overlap extension PCR using the cas9-mut-FWD and cas9-mid-REV or cas9-mid-FWD and cas9-mut-REV primers to create a Cas9 gene fragment with a single residue mutation. These Cas9 gene fragments were then each cloned back into PX165 using unique ApaI and EcoRI restriction sites to replace the wild-type sequence with the mutant sequence. Additional mutants (double-, triple-, quadruple-, and quintuple-mutants) were made iteratively starting from these single-mutant plasmids. A custom gRNA cloning backbone vector was created by PCR amplification from pX330 using the gRNA-scaffold-NheI-FWD and gRNA-scaffold-EcoRI-REV primers and restriction cloning into pUC19 (ThermoFisher) using NheI and EcoRI digestion. The gRNA spacer sequence oligos, listed in Supplementary Table 2, were phosphorylated with T4 polynucleotide kinase (NEB) and cloned into gRNA cloning backbone by Golden Gate cloning with BpiI digestion. PE2 prime editor was obtained from pCMV-PE2 and a cloning backbone for pegRNA expression was obtained from pU6-pegRNA-GG-acceptor, which were gifts from David Liu. The pegRNA oligos, listed in Supplementary Table 3, were phosphorylated with T4 polynucleotide kinase

(NEB) and cloned into pU6-pegRNA-GG-acceptor by Golden Gate cloning with Eco31I digestion. Primers were synthesized by IDT. Restriction enzymes were obtained from ThermoFisher. T7 DNA ligase was obtained from NEB. Plasmids were transformed into competent Stbl3 chemically competent *E. Coli* (ThermoFisher). Sequences for the wild-type Cas9, vCas9, and gRNA cloning backbone vectors are presented in the Sequences section.

Structure analysis

Crystal structures of Cas9 with substrate DNA bound (5F9R) or without substrate DNA bound (4ZT0) were analyzed using PyMol (Schrödinger).

Cell transfection

Cells were seeded in the maintenance medium without Pen-Strep into 24-well plates at 100,000 cells/well. Transfections of HEK293T without repair templates were carried out 24 hrs after seeding using 400 ng Cas9 expression vector and 144 ng gRNA expression vector formulated with 1.36 μL Lipofectamine 2000 (ThermoFisher) at a total volume of 54.4 μL in OptiMEM I (ThermoFisher) per well. Transfections of HEK293T, HeLa, A549, and Panc1 with HDR templates were carried out 24 hrs after seeding using 400 ng Cas9 expression vector, 144 ng gRNA expression vector, and 400 ng ssODN HDR template formulated with 2.11 μL Lipofectamine 2000 at a total volume of 84.4 μL in OptiMEM I per well. Transfections of HEK293T and primary human dermal fibroblasts with MDR vectors were carried out 24 hrs after seeding (HEK293T) or 7 days after quiescence induction (primary human dermal fibroblasts) using 400 ng Cas9 expression vector, 144 ng gRNA expression vector, and 153-295 ng (equimolar) MDR template formulated with 1.74-2.10 μL (equal volume / DNA) Lipofectamine 2000 at a total volume of 69.7-83.9 μL (equal DNA concentration) in OptiMEM I (ThermoFisher) per well. Transfections of HEK293T and primary human dermal fibroblasts with prime editing vectors were carried out 24 hrs after seeding (HEK293T) or 7 days after quiescence induction (primary human dermal fibroblasts) using 475 ng PE2 expression vector, 114 ng pegRNA expression vector, and 144 ng nicking gRNA expression vector (for PE3) formulated with 1.47-1.83 μL (equal volume / DNA) Lipofectamine 2000 at a total volume of 58.9-73.3 μL (equal DNA concentration) in OptiMEM I (ThermoFisher) per well. For sequencing assays, genomic DNA was extracted 72 hrs after transfection using QuickExtract (Epicentre). For flow cytometry assays, cells were transferred to 6-well plates 72 hrs after transfection, split 7 days after transfection, and harvested 10 days after transfection in PBS with 5% FBS (ThermoFisher). Repair templates, listed in Supplementary Table 4, were synthesized by IDT.

Next-generation sequencing

The targeted loci were amplified from extracted genomic DNA by PCR using Herculase II polymerase (Agilent). The PCR primers included Illumina sequencing handles as well as replicate-specific barcodes. These PCR products were then tagged with sample-specific barcodes and sequenced on an Illumina MiSeq. To measure mutational outcomes, the sequencing data were analyzed using Crispresso2 [25]. Primers, listed in Supplementary Table 5, were synthesized by IDT.

Sanger sequencing

The targeted loci were amplified from extracted genomic DNA by PCR using Herculase II polymerase (Agilent). PCR amplicons were sequenced using primers ~200 bp from the expected cut site. To measure precise editing and indel frequencies, the sequencing traces were analyzed using TIDER [19]. Primers, listed in Supplementary Table 6, were synthesized by IDT.

Cell cycle profiling

Primary human dermal fibroblasts were seeded in the maintenance medium without Pen-Strep into 12-well plates at 100,000 cells/well (dividing cells) or 200,000 cells/well (quiescent cells). Profiling was carried out 24 hrs after seeding (dividing cells) or 7 days after quiescence induction (quiescent cells). Cells were pulsed with 10 μM 5-ethynyl-2'-deoxyuridine (EdU) added to the medium for 1 hr before harvesting. Cells from four wells per condition were pooled, fixed, permeabilized, and stained for EdU incorporation using a Click-iT Plus EdU Alexa Fluor 647 Flow Cytometry Assay Kit (ThermoFisher). To label total DNA content, cells were resuspended in Click-iT saponin-based permeabilization and wash buffer (ThermoFisher) with 20 μg/mL propidium iodide and 100 μg/mL RNase A for 30 min. Cells were analyzed by flow cytometry to profile cell cycle stage.

Flow cytometry

Flow cytometry analysis was performed on an LSR Fortessa analyzer and data was collected using FACSDiva (BD Biosciences). Cells were first gated comparing SSC-A and FSC-A, then SSC-H and SSC-W, then FSC-H and FSC-W parameters to select for single cells. To assess editing frequencies, cells

were gated for GFP (488 nm laser excitation, 530/30 nm filter detection) and BFP (405 nm laser excitation, 450/50 nm filter detection). To profile cell cycle stage, cells were gated for propidium iodide (561 nm laser excitation, 610/20 nm filter detection) and Alexa Fluor 647 (640 nm laser excitation, 670/30 nm filter detection). Flow cytometry data were analyzed using FlowJo (FlowJo).

Quantification and statistical analysis

Specific statistical comparisons are indicated in the figure legends. Error bars indicate the standard error for up to three independent replicates. In most comparisons, significance was assessed using unpaired, two-tailed Student's t-tests. For correlations, significance was assessed using Pearson's tests. For linear regressions, significance was assessed using ANCOVA tests. Genome editing quantification was carried out using Crispresso2 [25] for next-generation sequencing data or TIDER for Sanger sequencing data [19]. Unedited cells were used as a reference for sequencing analysis. For repair mechanism analysis, next-generation sequencing reads were classified using annotated repair mechanisms determined by Indelphi [4]. Mean indel sizes were calculated as the mean of the absolute values of indel sizes weighted by their indel fractions. Next-generation sequencing data were normalized relative to the total number of reads for in each sample. Sanger sequencing-based TIDER data for the engineered Cas9 variant screen were normalized relative to the total editing activity (indels + precise) of wild-type Cas9 in each experiment.

Data and Materials Availability

Raw next-generation sequencing data are to be made available on NCBI SRA. Plasmids are to be deposited on Addgene.

References

1. Cong, L. *et al.* Multiplex genome engineering using CRISPR/Cas systems. *Science.* **339**, 819–823 (2013).

2. Mali, P. *et al.* RNA-guided human genome engineering via Cas9. *Science.* **339**, 823–826 (2013).

3. Allen, F. *et al.* Predicting the mutations generated by repair of Cas9-induced double-strand breaks. *Nat. Biotechnol.* (2019).

4. Shen, M. W. *et al.* Predictable and precise template-free CRISPR editing of pathogenic variants. *Nature* (2018).

5. Bunting, S. F. *et al.* 53BP1 inhibits homologous recombination in Brca1-deficient cells by blocking resection of DNA breaks. *Cell* **141**, 243–254 (2010).

6. Cannavo, E. & Cejka, P. Sae2 promotes dsDNA endonuclease activity within Mre11-Rad50-Xrs2 to resect DNA breaks. *Nature* **514**, 122 (2014).

7. Costelloe, T. *et al.* The yeast Fun30 and human SMARCAD1 chromatin remodelers promote DNA end resection. *Nature* **489**, 581 (2012).

8. Sartori, A. A. *et al.* Human CtIP promotes DNA end resection. *Nature* **450**, 509 (2007).

9. Zimmermann, M., Lottersberger, F., Buonomo, S. B., Sfeir, A. & de Lange, T. 53BP1 regulates DSB repair using Rif1 to control 5′ end resection. *Science.* **339**, 700–704 (2013).

10. Chapman, J. R., Taylor, M. R. G. & Boulton, S. J. Playing the end game: DNA double-strand break repair pathway choice. *Mol. Cell* **47**, 497–510 (2012).

11. Symington, L. S. & Gautier, J. Double-strand break end resection and repair pathway choice. *Annu. Rev. Genet.* **45**, 247–271 (2011).

12. Shou, J., Li, J., Liu, Y. & Wu, Q. Precise and Predictable CRISPR Chromosomal Rearrangements Reveal Principles of Cas9-Mediated Nucleotide Insertion. *Mol. Cell* (2018).

13. Gasiunas, G. *et al.* A catalogue of biochemically diverse CRISPR-Cas9 orthologs. *Nat. Commun.* **11**, 5512 (2020).

14. Liang, Z., Sunder, S., Nallasivam, S. & Wilson, T. E. Overhang polarity of chromosomal double-strand breaks impacts kinetics and fidelity of yeast non-homologous end joining. *Nucleic Acids Res.* **44**, 2769–2781 (2016).

15. So, C. C. & Martin, A. DSB structure impacts DNA recombination leading to class switching and chromosomal translocations in human B cells. *PLOS Genet.* **15**, e1008101 (2019).

16. Jiang, F. *et al.* Structures of a CRISPR-Cas9 R-loop complex primed for DNA cleavage. *Science.* **351**, 867–871 (2016).

17. Kleinstiver, B. P. *et al.* High-fidelity CRISPR–Cas9 nucleases with no detectable genome-wide off-target effects. *Nature* **529**, 490–495 (2016).

18. Slaymaker, I. M. *et al.* Rationally engineered Cas9 nucleases with improved specificity. *Science.* **351**, 84–88 (2016).

19. Brinkman, E. K. *et al.* Easy quantification of template-directed CRISPR/Cas9 editing. *Nucleic Acids Res.* (2018).

20. Chu, V. T. *et al.* Increasing the efficiency of homology-directed repair for CRISPR-Cas9-induced precise gene editing in mammalian cells. *Nat. Biotechnol.* **33**, 543–548 (2015).

21. Orthwein, A. *et al.* A mechanism for the suppression of homologous recombination in G1 cells. *Nature* **528**, 422 (2015).

22. Truong, L. N. *et al.* Microhomology-mediated End Joining and Homologous Recombination share the initial end resection step to repair DNA double-strand breaks in mammalian cells. *Proc. Natl. Acad. Sci.* (2013).

23. Mitra, M., Ho, L. D. & Coller, H. A. An In Vitro Model of Cellular Quiescence in Primary Human Dermal Fibroblasts. *Methods Mol. Biol.* **1686**, 27–47 (2018).

24. Anzalone, A. V *et al.* Search-and-replace genome editing without double-strand breaks or donor DNA. *Nature* **576**, 149–157 (2019).

25. Clement, K. *et al.* CRISPResso2 provides accurate and rapid genome editing sequence analysis. *Nat. Biotechnol.* **37**, 224–226 (2019).

Acknowledgements

The authors thank Salil Garg, Dig Bijay Mahat, Luke Rhym, and Amanda Whipple for helpful discussions. This research was supported by a grant from the Lustgarten Foundation, by a grant from the Life Sciences Research Foundation, by a grant (R01-CA208205) from the National Cancer Institute, and partially by a Cancer Center Support (core) Grant (P30-CA14051) from the National Cancer Institute. V.P.C. is a Fellow of the Life Sciences Research Foundation.

Author Contributions

V.P.C., P.A.S., and R.L. conceived or designed the work; V.P.C., P.A.S., and R.L. acquired, analyzed, or interpreted the data; V.P.C., P.A.S., and R.L. drafted the work or substantively revised it.

Competing Interests

The authors have filed for a patent related to this work.